Journal of Marine Science and Technology (2020) 25:520–535
https://doi.org/10.1007/s00773-019-00658-9

ORIGINAL ARTICLE

Numerical study on coupled effect of a vessel loaded with liquefied nickel ore

Jianwei Zhang[1] · Wanqing Wu[2] · Zihao Zhao[2] · Yulong Chen[3]

Received: 16 April 2018 / Accepted: 28 May 2019 / Published online: 4 June 2019

Abstract
Liquefaction of granular bulk cargo could result in cargo movement and loss of stability of ships, causing the loss of many lives in marine casualties in recent years. To ensure shipping safety, experimental tests and numerical methods have been adopted to reveal the coupled mechanism between liquefied cargo movement and ship motions. In the present study, a numerical model based on a CFD solver and non-Newtonian constitutive equations was established to solve the sloshing of liquefied nickel ore. Validations were carried out by comparing with available experimental data. A nonlinear simplified body surface method is proposed for the external ship response. The two problems are coupled through a coupling strategy. Different wave frequencies and amplitudes were considered and analyzed. Finally, the main reasons for the ship capsizing were deduced and concluded.

Keywords Liquefaction · Coupled effect · VOF method · Time domain simulation · Capsize

1 Introduction

According to the International Maritime Solid Bulk Cargoes (IMSBC) code [1], a number of granular bulk cargoes have been classified as 'Group A' cargoes, which have the potential to liquefy due to the proportion of fine particles and moisture they contain. For instance, nickel ore and iron ore fines are the two most widely known solid bulk cargoes with this hazard, which are widely distributed all over the world like Indonesia, Philippines and New Caledonia. When the moisture content is higher than the transportable moisture limit (TML) combined with excitations from ship motions and vibration of machineries on board, the cargo may liquefy and behave like a fluid. Lee [2] pointed out that even when the moisture content is smaller than its TML, whether the liquefaction happens or not is still uncertain. Owing to its high density and viscosity after liquefaction, its sloshing behavior would have a great impact on the motion and stability of the ship. Ship capsizing would happen, especially in some unwanted seas. In the last 2 decades, more than 800 seamen have lost their lives on bulk carriers [3]. From 2001 to 2010, more than 23 ships carrying solid bulk cargoes sunk in China [4]. For further recommendations and arrangements to be proposed to prevent ship capsizing, the coupled effect of the liquefied cargo sloshing on the rolling response of a ship should be investigated in advance.

However, due to the complexity of the liquefaction process, the study on the coupled case of liquefied cargo and ship motions has not been fully developed. Backalov [5] and Vassalos [6] stated that a limited number of contributions have been provided on the topic of granular materials which are different from a perfectly solid or a perfectly Newtonian fluid cargo. Several studies relevant to the problem are summarized as follows. Model tests have been carried out by Koromila et al. [7] to investigate the liquefaction of granular materials under roll and sway excitations using shaking table facilities. Results show that the ship stability would be reduced when cargo liquefaction happens. Using the method of molecular dynamics, Spandonidis and Spyrou [8] solved the coupled motions of granular material and vessel in regular beam seas, assuming that the cargo particle is dry and spherical. It is found that as a result of significant cargo movement, the barge cannot return towards the upright

✉ Wanqing Wu
wuwanqingdmu@sina.com

[1] School of Port and Transportation Engineering, Zhejiang Ocean University, Zhoushan, China

[2] School of Marine Engineering, Dalian Maritime University, Dalian, China

[3] State Key Laboratory of Hydroscience and Engineering, Tsinghua University, Beijing, China

position and capsize is finally realized at higher wave amplitudes. Ju et al. [9] addressed a solid bulk cargo–sea–ship problem by solving the rolling response of a 2D rectangular hold in regular waves. Effect of moisture content is replaced by corresponding friction coefficients. The discrete element method (DEM) code was used to simulate movement of the cargo and the numerical wave tank was adopted to solve the motion of the hold. The moment induced by movement of the cargo is included in their coupled mode. They concluded that the cargo with higher moisture content has lower friction coefficient and lead to the high risk of capsizing. To address the effect of liquefied cargo on the motion response of a vessel, mainly the numerical method was adopted and the assumption is always made in the current literature. The behavior of actual liquefied cargo has not been addressed extensively. And the problem is in fact a coupled one. Both of the impact forces and the weaken effect on the stability of a ship should be considered.

There has been a considerable amount of work on the coupled problem between liquid sloshing and vessel motions for Newtonian fluids. Faltinsen and Timokha [10] have offered a textbook to deal with the overall aspects of sloshing. For the coupled motion, Kim et al. [11] studied the anti-rolling tank problem. The finite-difference method is adopted to simulate the sloshing flow and the ship motion is obtained by a time-domain panel method. Kim et al. [12] and Lee et al. [13] considered the coupling effects of ship motion and sloshing and found that the nonlinearity of sloshing flow is very important in coupling analysis. Li et al. [14] and Jiang et al. [15] considered the coupling effects between tank sloshing and ship motions based on a CFD platform OpenFOAM. Results show that the moment phase difference between the wave excitation and sloshing-induced moment makes the dramatic reduction of the roll motion when the encounter frequency is in the resonance range. Based on model experiments, Rognebakke and Faltinsen [16] conducted two-dimensional experiments of a hull section containing tanks partially filled with water excited by regular waves. It is revealed that, even if violent sloshing occurs in the tank, the steady-state motion is almost linear and sinusoidal. Nasar et al. [17] investigated the interaction between the liquid sloshing and a barge through an experimental program. A split up of roll resonance was observed for the aspect ratio of 0.163 due to the coupling effect. Zhao et al. [18, 19] investigated the effects of sloshing on the global motion responses of a floating liquefied natural gas (FLNG) vessel through model tests. They concluded that the effects of the tank sloshing on the motions of FLNG were sensitive to wave excitation frequencies.

In general, plenty of works have been done to deal with coupled problems of liquid sloshing and vessel motions. With regard to liquid water and LNG sloshing, the impact forces and structural damage are always the big concerns. Aside from that, the granular bulk cargo after liquefaction behaves more like a non-Newtonian fluid. Not only the sloshing impact but also the effect on the stability of a ship should be considered in the coupled analysis. In the present study, the nickel ore with a moisture content of 40% is used and it is assumed as a non-Newtonian fluid after liquefaction. A numerical model based on a CFD solver and non-Newtonian constitutive equations was proposed to solve the liquefied cargo sloshing. The motions of a vessel subject to regular transverse waves were solved by a nonlinear simplified body surface method. The cargo sloshing and the vessel motions are coupled through an explicit coupling strategy. To validate the present numerical model and the coupling strategy, the uncoupled case of liquefied nickel ore sloshing and coupled case of liquid water sloshing were carried out and compared. Finally, the coupled effect of liquefied nickel ore sloshing on the motion and stability of a vessel was discussed and the main reasons for the ship capsizing were deduced and concluded.

2 Mathematic formulation and numerical approach

2.1 Sloshing problem of liquefied cargo

The liquefied nickel ore is assumed as non-Newtonian, incompressible and inelastic. The flow of non-Newtonian fluid is assumed as laminar and isothermal. The turbulent effects are not taken into account in the present research. The continuity and the momentum conservation equations governing the flow are written as follows:

$$\frac{\partial u_i}{\partial x_i} = 0, \tag{1}$$

$$\rho\frac{\partial u_i}{\partial t} + \rho u_j\frac{\partial u_i}{\partial x_j} = -\frac{\partial p}{\partial x_i} + \frac{\partial}{\partial x_j}\left[\mu\left(\frac{\partial u_i}{\partial x_j} + \frac{\partial u_j}{\partial x_i}\right)\right] + F_i. \tag{2}$$

Here x_i are Cartesian coordinates, u_i are the corresponding velocity components. $\rho = \alpha\rho_1 + (1-\alpha)\rho_2$ is the mixture density. ρ_1 and ρ_2 are the density of liquefied nickel ore and the air, respectively. $\mu = \alpha\mu_1 + (1-\alpha)\mu_2$ is the mixture viscosity. μ_1 and μ_2 are the viscosity of liquefied nickel ore and the air, respectively. α is the fluid volume fraction, which is set to 1 in the fluid region, 0 in the air region and between 0 and 1 for the interface. F_i is the external body force and p is the pressure.

Volume of fluid (VOF) method is adopted to capture the free surface. For each phase a variable, α, the volume fraction of the corresponding phase is introduced. Deformation of the interface is characterized by means of a scalar

function, whose value is set based on the volume fraction of a computing unit. At each time step, the function is solved to find the distribution of the fluid phases. The equation governing α is as follows:

$$\frac{\partial \alpha}{\partial t} + u_i \frac{\partial \alpha}{\partial x_i} = 0. \tag{3}$$

For Newtonian fluid, the stress tensor follows the Newtonian law and its viscosity can be expressed as a linear and explicit stress–strain relationship. The viscosity of non-Newtonian inelastic fluid is a function of shear rate magnitude. The rheological constitutive equation of generalized Newtonian fluids is expressed as follows:

$$\tau = \mu(\dot{\gamma})\dot{\gamma}. \tag{4}$$

Here τ is the stress tensor, $\dot{\gamma}$ is the shear rate tensor.

After the nickel ore with moisture is liquefied, it is a mixture of fine ore particles and liquid water. As the moisture content increases, the liquefied cargo becomes increasingly muddy in appearance. And its rheology characteristics belong to non-Newtonian fluids [20, 21]. At low shear rates, the liquefied nickel ore exhibited a yield stress and has a shear thinning behavior, which can be described by the Herschel–Bulkley equation. At higher shear rates, the gradient of the rheogram becomes constant, the mixture can be modeled as a Bingham plastic fluid [22–24]. In the present study, the Herschel–Bulkley and the Bingham equations are adopted to describe the rheological property of the liquefied nickel ore. The viscosity of the nickel ore slurry is defined by its apparent viscosity ($\mu_A = \tau/\dot{\gamma}$). The rheological constitutive equation is expressed as follows:

$$\begin{cases} \mu_A = \mu_y, \text{ when } 0 \le \dot{\gamma} \le (\tau_{yHB}/\mu_y) \\ \mu_A = \dfrac{\tau_{yHB}}{\dot{\gamma}} + K_{HB}\dot{\gamma}^{(n_{HB}-1)}, \text{when } (\tau_{yHB}/\mu_y) < \dot{\gamma} \le (\tau_{yBing}/\mu_y) \\ \mu_A = \dfrac{\tau_{yBing}}{\dot{\gamma}} + K_{Bing}, \text{ when } (\tau_{yBing}/\mu_y) < \dot{\gamma}. \end{cases} \tag{5}$$

Here μ_y represents a constant high yielding viscosity for shear rates below the yield stress, at which stage the mixture acts essentially like a solid. τ_{yHB}, K_{HB} and n_{HB} are the yield stress, the consistency index and the power-law index of the Herschel–Bulkley equation respectively. τ_{yBing}, and K_{Bing} are the yield stress and the plastic viscosity of the Bingham plastic equation.

Assuming that the flow is laminar, Eqs. 1–3 and 5 fully describe the sloshing problem of liquefied nickel ore when an accurate set of initial and boundary conditions is imposed. The dimensionless shear rate is obtained by the velocity field of the previous time step, and the apparent viscosity field of the mixture is calculated through the constitutive equations. With the process described above, the dynamical behavior of non-Newtonian fluid is solved in the same way as for a Newtonian fluid with a changing viscosity.

The three-dimensional, laminar, pressure-based solver is used to solve the incompressible flow on the collocated grid arrangement. The second-order upwind scheme is used to discretize convective terms of momentum equations. The semi-implicit method for the pressure-linked equations (SIMPLEC) [25] scheme is adopted for solving the pressure–velocity decoupling. The Gauss–Seidel point-by-point iterative method is used for solving the algebraic equations. The CFD solver, ANSYS/Fluent 13.0 [26] is used for the sloshing simulations.

2.2 Large amplitude roll motion of a vessel

To account for the nonlinearity caused by the variation of the instantaneous wetted surface and the computational efficiency, a nonlinear simplified body surface method is adopted. Gao et al. [27] have used a similar method to study the hydrodynamics of a flooded ship. The hydrodynamic coefficients of a vessel considering the instantaneous wetted body surface are pre-calculated in the frequency domain and stored based on the database technique. During the time simulation, their instantaneous values are transmitted from the stored values according to the positions of the vessel at each instant and substituted into the time domain equation, the large amplitude motion of a vessel could be solved. Based on the Newton's Second Law, the equation reflecting a vessel's 6-DOF motions in time domain has a form as [28, 29]:

$$\sum_{j=1}^{6}\left[\left(m_{ij} + a_{ij}(\infty)\right)\ddot{x}_j(t) + \int_0^t R_{ij}(t-\tau)\dot{x}_j(\tau) + b_{ij}\dot{x}_j(t) + c_{ij}x_j(t)\right] = F_i(t)\,(i = 1, \ldots, 6). \tag{6}$$

Here $a_{ij}(\infty)$ and b_{ij} are the added mass at infinite frequency and damping coefficients, respectively. m_{ij} is the mass matrix of a vessel. R_{ij} is the retardation function representing the time memory effect. c_{ij} is the restoring coefficient and $F_i(t)$ is the sum of incident force and diffraction force. For the large amplitude motion, we assume as a first approximation that the effect between different positions of a vessel is not significant, and thus the time memory effect is not considered.

As the restoring and incident forces are the main parts of the external wave forces, the two forces should be calculated exactly considering the instantaneous wetted surface. And they are given as follows:

$$F_{S+FK}(t) = -\iint_{S_B(t)} (p_s + p_{FK}) n_j \mathrm{d}S. \tag{7}$$

Here F_{S+FK} represents the sum of restoring and Froude–Krylov forces, $S_B(t)$ is the instantaneous wetted surface of the vessel corresponding to the incident wave. p_s and p_{FK} are the hydrostatic pressure and the incident wave pressure, respectively.

In the present study, the hydrodynamic coefficients of a floating vessel in frequency domain are calculated by the OpenSource BEM solver NEMOH. It is a linear diffraction and radiation solver developed by the Ecole Centrale de Nantes [30]. It has been adopted by Sheng et al. [31] and Pal Schmitt et al. [32] to assess the hydrodynamic performance of a floating structure. With user-defined boundary conditions such as water depth, motion frequency and position of rotation axis, the hydrodynamic coefficients could be acquired.

2.3 Coupling strategy in time domain

In Sects. 2.1 and 2.2, the sloshing and sea-keeping solvers are independently developed and compiled. Therefore, the development of a communication strategy between the two solvers is also a key point of the work. Hashimoto et al. [33] have studied the coupling of tank fluid and ship roll motions by numerical simulations. And the sloshing-induced force is included in the right side of the motion equation as an external excitation. For the liquefied cargo, its weaken effect on vessel stability is included in the hydrodynamic coefficients by carrying out numerical tilting tests. Compared to the method used by Ju et al. [9], both the sloshing-induced moment and the weaken effect are included in the present study. And for the numerical wave tank adopted in Ref. [9], the ship motion equation solved by user-defined function (UDF) has a better computational efficiency. Thus, the coupled roll motion equation of a floating vessel containing a liquefied cargo tank in the time domain can be written as:

$$\begin{aligned}&\left(m_{44}+a_{44}^{'}\right)\ddot{x}_4(t)+b_{44}^{'}\dot{x}_4(t)+b_{44}^{\mathrm{v}}\left|\dot{x}_4(t)\right|\dot{x}_4(t)\\&\quad+c_{44}^{\mathrm{cargo}}x_4(t)=F_4^{'}(t)+F^{\mathrm{slosh}}(t).\end{aligned}\tag{8}$$

Here $x_4(t)$ is the angular displacement of the roll motion, $a_{44}^{'}$ and $b_{44}^{'}$ are the added mass coefficient and linear damping coefficient taking into account the variation of the wetted surface, b_{44}^{v} is the viscous damping coefficient, c_{44}^{cargo} is the restoring coefficient considering the weaken effect of the liquefied cargo movement and it was estimated by a series of numerical tilting tests. $F_4^{'}(t)$ and $F^{\mathrm{slosh}}(t)$ are the external wave forces and the sloshing-induced forces, respectively.

The coupling strategy can be performed according to Eq. 8 and its flow chart is shown in Fig. 1. After solving Eq. 8 at t instant, the vessel response is obtained and adopted as the moving-wall boundary conditions for the internal sloshing at $t+\mathrm{d}t$ instant. Then from the solution of the sloshing problem, the sloshing-induced forces are obtained. The sloshing forces together with the wave forces are substituted into Eq. 8. The coupled motion of the vessel at $t+dt$ instant can be achieved. And the coupled motion response of the vessel would be used as the known conditions for sloshing at the next time step. Until the simulation time reaches the desired one, time histories of the coupled motion including sloshing can be acquired. In the present study, the coupling strategy is proposed based on the UDF provided by the ANSYS/Fluent platform. The same time step is adopted for solving the internal sloshing and the vessel motion. The simulations are accomplished in an Intel (R) i7 CPU @2.93 GHz & 3.07 GHz desktop PC with 4.0 GB of RAM.

3 Numerical validations

3.1 Sloshing of liquefied nickel ore under forced excitations

A prismatic cargo hold model that originates from a 57,000 DWT bulk carrier is investigated here. For efficiency, only the internal structure is investigated. The scale is 1:66. Figure 2 shows the sizes of the cargo hold model and the mesh arrangement. For all cases, the cargo depth (d) is 121 mm above the bottom and the length is 150 mm.

The cargo hold undergoes a forced roll motion around its roll center, located 80 mm above its bottom. The motion follows a sinusoidal function given as $\theta = A\sin(\omega t)$, where A and ω are the rolling amplitude and the frequency, respectively. The rolling amplitude are chosen as 7° and 10°, while the excitation periods are 1.57 s and 4 s, respectively. The nickel ore slurry with 40% moisture content is adopted. Corresponding to Eq. 5, the constants derived from fitting the experimentally measured rheology to each non-Newtonian model are shown in Table 1.

The hexahedron gird is used for the simulation. The refinement process is applied to the boundary layer and near the free surface to capture the interface more accurately. The nickel ore slurry is assumed to be a single-phase fluid of uniform rheology using UDF to define its apparent viscosity. The no-slip wall condition is imposed on the entire boundaries. The dynamic mesh technique is utilized to handle the cargo's roll motion and the motion is specified in advance. Based on the new positions of the boundaries, the mesh is updated for each set of successive iteration.

Three different grids and time steps are adopted to carry out grid and time step sensitivity tests, shown in Table 2. The simulation is carried out for duration of ten periods. Figure 3 shows the variations of the sloshing-induced moment for different time steps, revealing that the results are close when the time step is 0.005 s and 0.002 s. For efficiency, the time step of 0.005 s is selected for the following simulations. Then, three different grid systems of coarse, medium and fine grids are checked. Results are shown in Fig. 4, in which it can be seen that the three grids give nearly the same outcome. To capture the free

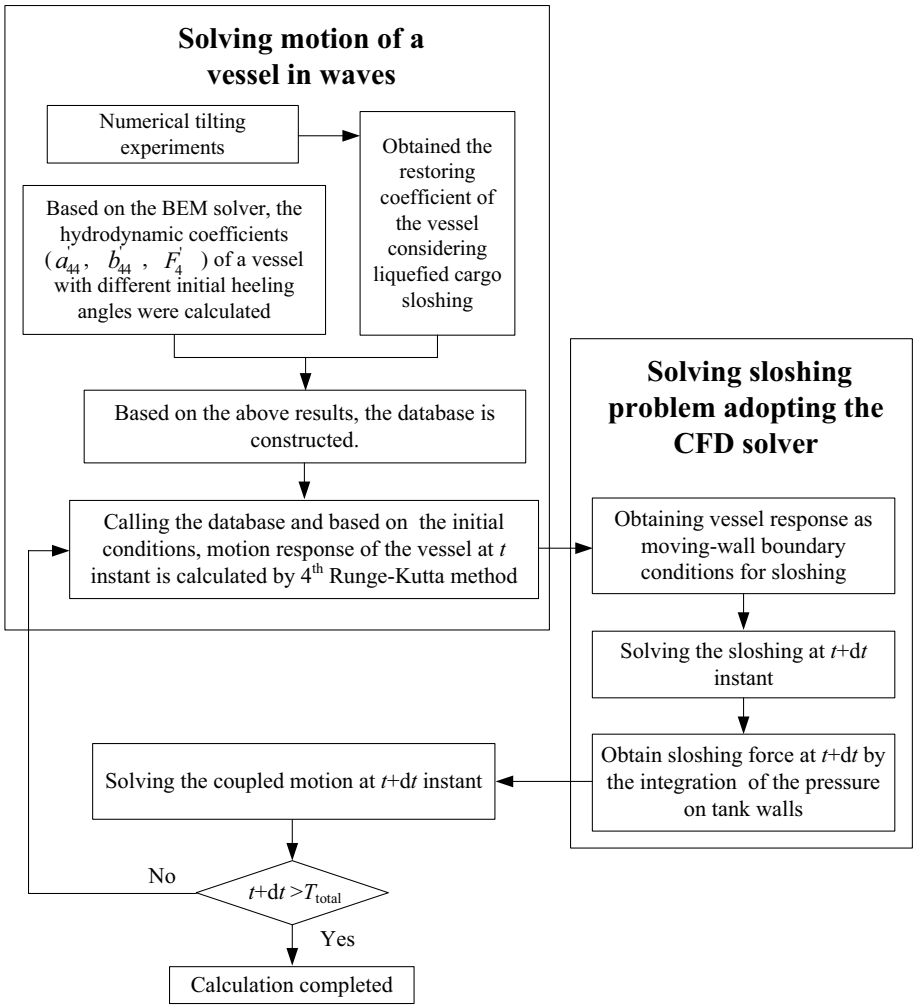

Fig. 1 Flow chart of the coupling strategy for solving the motion of a vessel including liquefied cargo sloshing

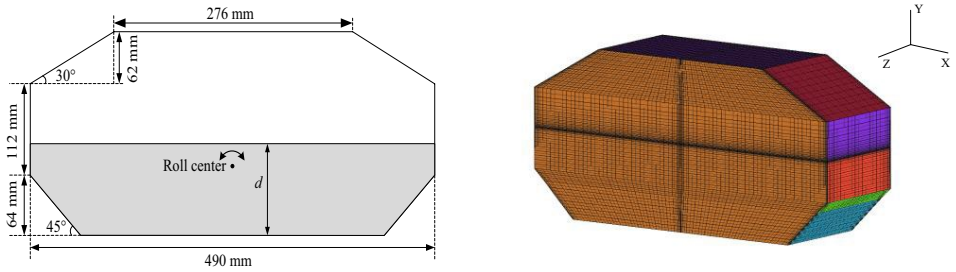

Fig. 2 Sketches of the cargo hold model and the mesh arrangement

Table 1 Density and rheology model parameters for nickel ore slurry with 40% moisture content

Parameters	ρ_1 (kg/m^3)	τ_{yHB} (Pa)	K_{HB} (kg/m s)	n_{HB}	τ_{yBing} (Pa)	K_{Bing} (kg/m s)
Nickel ore slurry with 40% moisture content	1667	4.741	3.774	0.565	52.18	0.0742

surface efficiently and accurately, the medium grid system is chosen for the simulation.

Under the same condition, the physical model experiments were carried out by Chen [34] using the nickel ore with 40% moisture content. Shown in Fig. 5, the cargo is loaded into a cargo hold model, which is forced to roll around its rolling center. The sloshing-induced moment is obtained by the data acquisition system. The comparisons are shown in Figs. 6, 7, and 8. The sloshing-induced moment behaves almost periodically. Both the amplitude and period of the moment of the

Table 2 Parameters used for grid and time step sensitivity tests

/	Grid	Time step (s)
Items	Coarse (1.52 MB, 12,240 elements) Medium (2.92 MB, 23,400 elements) Fine (5.36 MB, 42,500 elements)	0.01/0.005/0.002

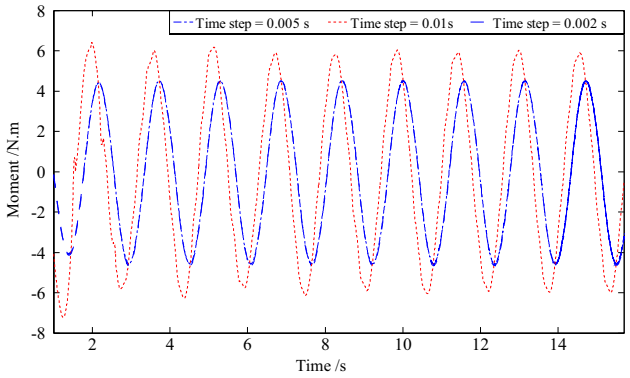

Fig. 3 Comparison of sloshing-induced moment computed with three different time steps

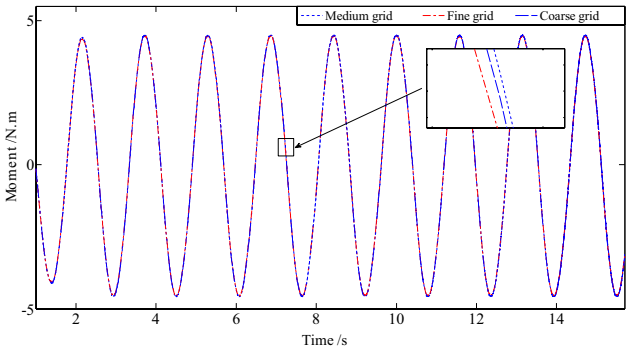

Fig. 4 Comparison of sloshing-induced moment computed with three different grid systems

simulation results basically agree well with the experimental data, however, the experimental data show more nonlinear effects and the numerical results behave more like trigonometric functions. The main reason lies in the deviation between the rheological constitutive equation of the liquefied cargo adopted in the present study and the actual one which is more complex due to the complicated liquefaction process of the granular bulk cargo. In reality, the mixture of the fine ore particles and liquid water is not homogeneous and layers with different characteristics would appear [35, 36]. And that would affect the magnitude and period of the sloshing-induced moment directly. Besides, the numerical dissipations and the probable measurement errors in the experiments are also the reasons.

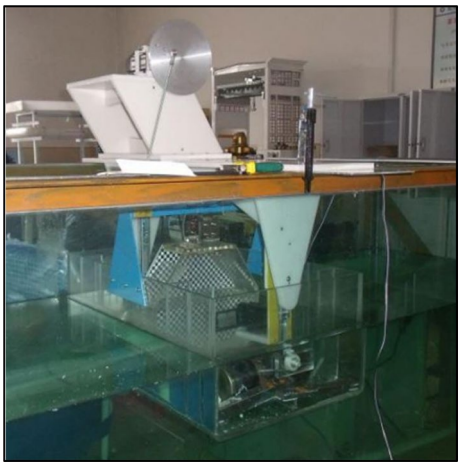

Fig. 5 The test system for liquefied nickel ore sloshing carried out by Chen [34]

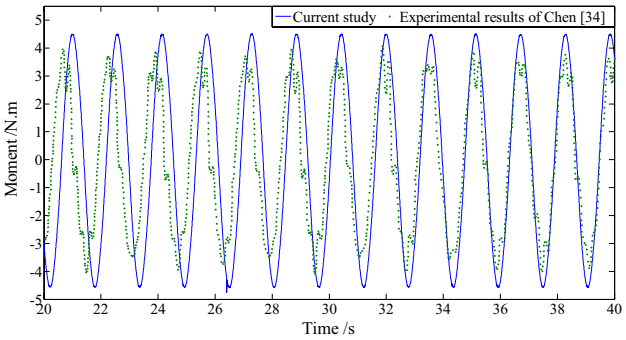

Fig. 6 Comparison of sloshing-induced moment with the experimental results, $A = 10°, T = 1.57$s

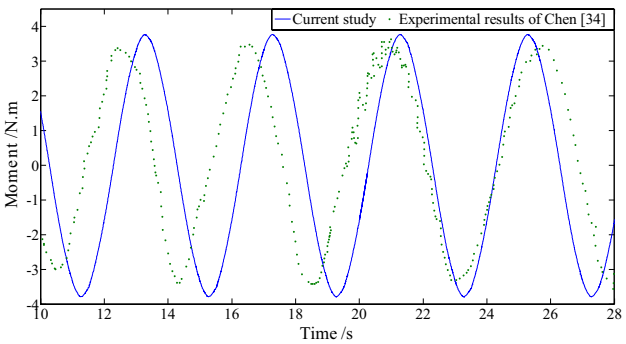

Fig. 7 Comparison of sloshing-induced moment with the experimental results, $A = 10°, T = 4$s

3.2 Coupled motion of a hull section partially filled with liquid water

To verify the coupling strategy shown in Fig. 1, a hull section partially filled with liquid water is investigated here. The

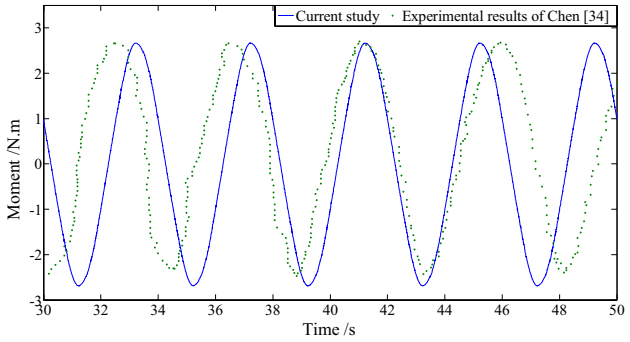

Fig. 8 Comparison of sloshing-induced moment with the experimental results, $A = 7°, T = 4$s

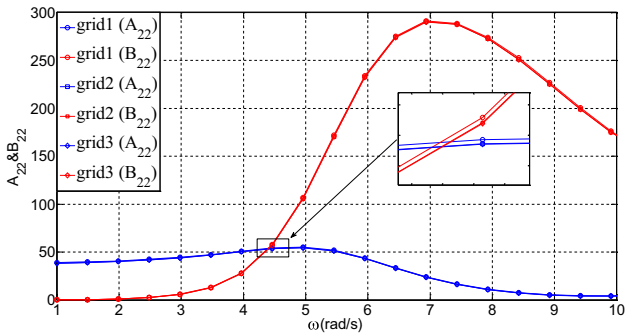

Fig. 9 Comparison of the added mass and linear damping coefficients under three different grid systems

Table 3 Data for hull section excluding internal fluid mass

Items	Without water	One tank with water
Filling height (m)	0	0.186
Mass of hull section (kg)	47.01	37.01
Natural frequency of fluid (rad/s)	/	8.658

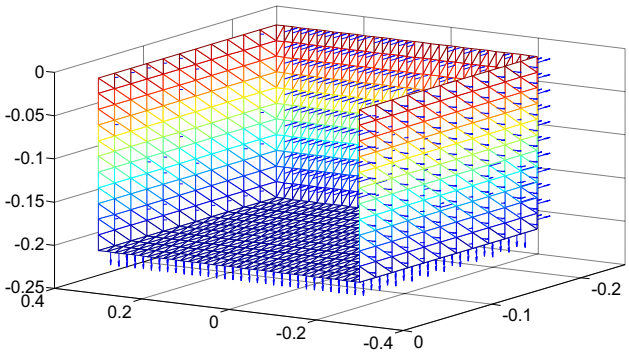

Fig. 10 Mesh adopted in the BEM calculation

experiments were carried out in a wave flume at Norwegian University of Science and Technology by Rognebakke and Faltinsen [16]. The horizontal rails were fixed on top of the flume and the hull section is only allowed to move in the direction of sway motion by sliding along the rails. The hull section contains two identical tanks and has a draft of 0.2 m. In the present study, one tank containing water is considered and the other conditions are the same as the experiment. The mass of the hull section excluding internal fluid mass is shown in Table 3.

During the analysis, to avoid the transient effects at the initial stage of the simulation, a ramp function is applied and it has a form as follows:

$$\text{Ramp} = \begin{cases} 1 & t > 2T \\ \frac{1}{2}\left(1 - \cos\left(\frac{\pi t}{2T}\right)\right), & t \le 2T \end{cases}. \tag{9}$$

Based on the coupling strategy, the wave–body interaction is solved first. Three different grid systems with 496 (grid1), 946 (grid2) and 1800 (grid3) surface elements were used to carry out the grid sensitivity tests, comparisons are shown in Fig. 9. When the surface elements of the grid are larger than 496, the results tend to converge. And the medium grid is adopted in the present study, as shown in Fig. 10. When the tank is empty, the calculated RAO of the section's sway motion and the comparison with experimental data are shown in Fig. 11. It can be seen that, the potential solver adopted in the present study is reliable and accurate. And this provides a better foundation for the analysis of the coupled motion including the internal sloshing.

Considering one tank of the hull section is partially filled with water, the filling height is 0.186 m. The incident wave frequency ranges from 7.0360 rad/s to 11.0561 rad/s. After carrying out the grid and time step independence study, the grid system (2.89 MB, 16,000 elements) and the time step 0.001 s are chosen for the sloshing simulation. Taking four different wave frequencies, for example, time histories of the sway motion considering water or not and the comparison of the internal sloshing force and the external wave force are presented in Figs. 12, 13, 14, and 15. The present results and the experimental data of the coupled sway motion RAO are shown in Fig. 16. From the results, it can be deduced that the sloshing effect on the coupled motion is both decided by the magnitude of the sloshing force and the phase difference between sloshing force and external wave force. When the phase difference equals π, time histories of the two forces are in anti-phase and the overall forces exerted on the hull section are the difference of the above two. When the wave frequency is far smaller than the fluid natural frequency, the sloshing-induced force is much smaller than the

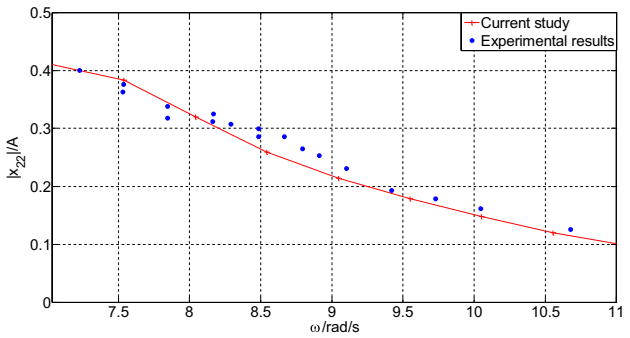

Fig. 11 Numerical and experimental results of sway motion for the hull section without water

wave force and the sloshing has little effect on the coupled motion. Combined with the phase difference at the same time, the amplitude of the coupled motion is a little smaller than the case without sloshing. See Fig. 12, as the wave frequency increases to near the resonance frequency, the sloshing-induced force grows bigger and the phase difference gets close to anti-phase. Therefore, the bigger sloshing force combined with the phase difference can decrease the amplitude of the coupled motion. When the wave frequency is around 8.5 rad/s, the amplitude of the coupled motion is the smallest. As the wave frequency increases further, both the amplitude of the sloshing force and the phase difference decrease. The amplitude of the coupled motion increases and it is obviously larger than the case without sloshing.

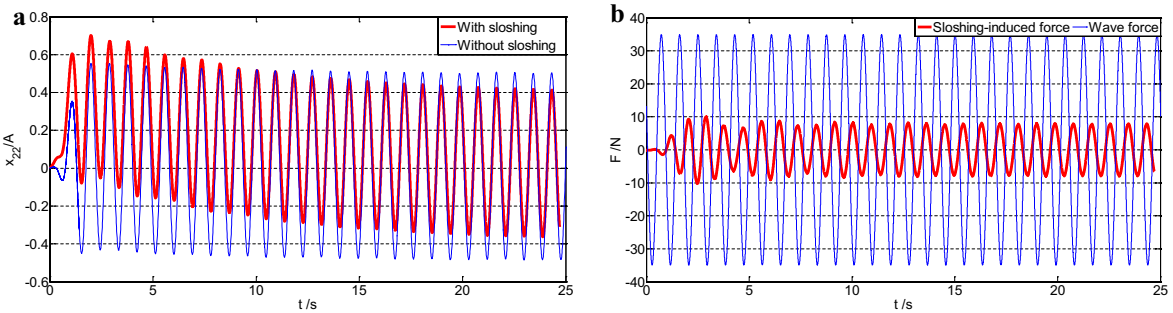

Fig. 12 Time history of the sway motion (**a**) and the comparison between wave force and internal sloshing force (**b**) when $\omega = 7.0360\,\mathrm{rad/s}$

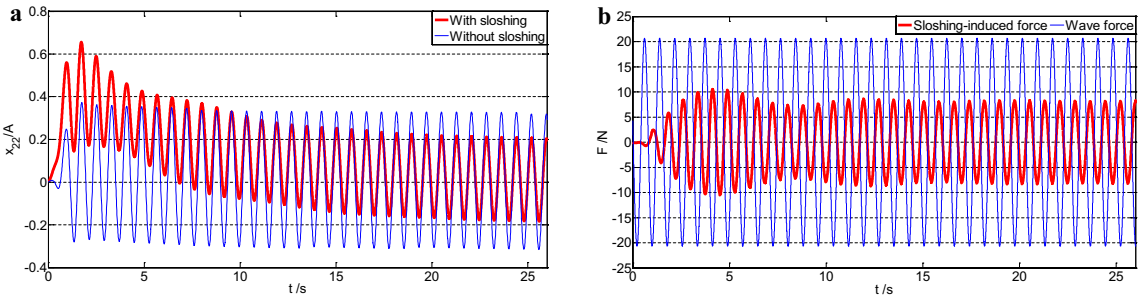

Fig. 13 Time history of the sway motion (**a**) and the comparison between wave force and internal sloshing force (**b**) when $\omega = 8.0410\,\mathrm{rad/s}$

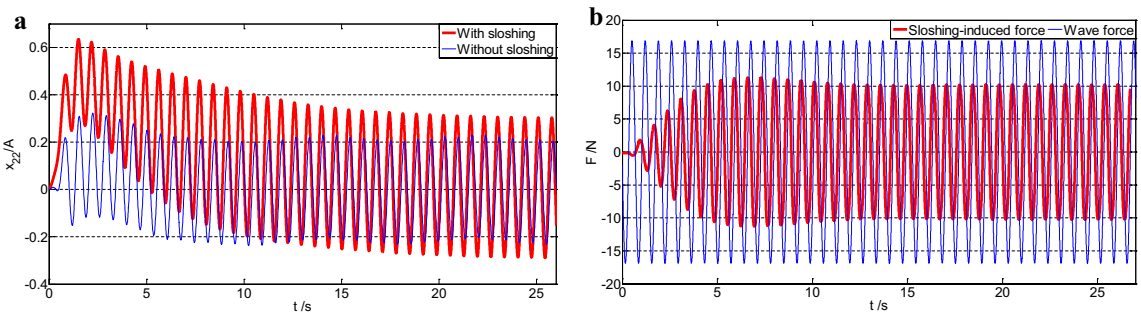

Fig. 14 Time history of the sway motion (**a**) and the comparison between wave force and internal sloshing force (**b**) when $\omega = 9.0460\,\mathrm{rad/s}$

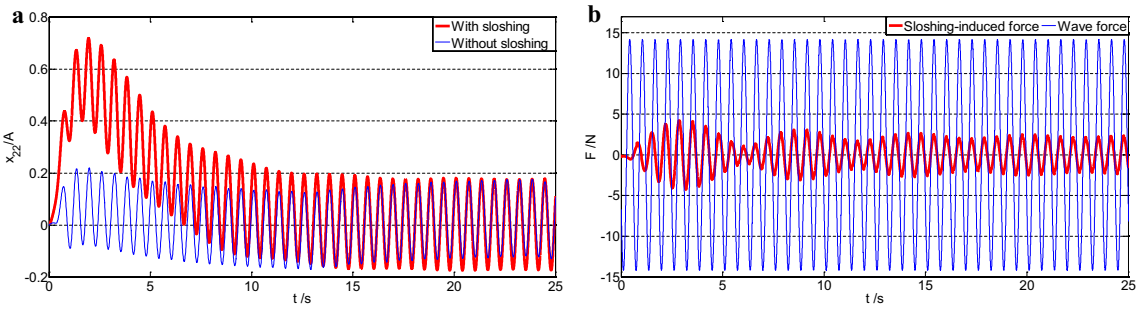

Fig. 15 Time history of the sway motion (left) and the comparison between wave force and internal sloshing force (right) when $\omega = 10.0511\,\mathrm{rad/s}$

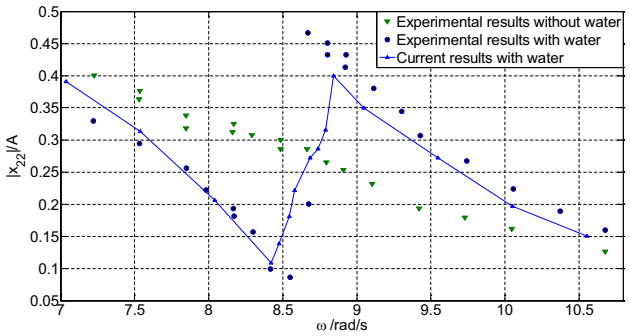

Fig. 16 The sway motion RAO of the hull section with or without water

And then the sloshing-induced force decreases monotonically. And the amplitude of the coupled sway motion also decreases and gets closer to the case without sloshing. In general, the present simulation results agree well with the experimental data except the peak position. The main reason lies in that the strong nonlinear physical phenomena such as wave impact and wave breaking occur near the resonance frequency of the sloshing fluid in actual situation. These phenomena would produce larger energy dissipation which would have great influence on the motions of the liquid tank. Due to the numerical dissipation and the approximate treatment of the free surface in the VOF method, there are some deviations in the simulation of the sloshing under resonance condition.

4 Coupled effect of liquefied cargo sloshing on rolling response of a vessel

4.1 Model configuration

The coupled effect of liquefied cargo sloshing on the roll motion is investigated based on a box-type vessel (see Fig. 17). The vessel is divided into three tanks. Tank II is a prismatic cargo hold loaded with liquefied nickel ore. Its sizes are shown in Fig. 17. The other two tanks are empty. The rheology parameters of the liquefied nickel ore are presented in Table 1. The specific parameters for the calculation are illustrated in Table 4. Considering that the coupled effect is more pronounced in the mode of roll motion, the roll motion in regular beam waves is investigated here. During the simulation, it is assumed that the vessel can only rotate around its center of gravity.

For the roll motion of the vessel, the viscous effect in the direction of rotation should be taken into account. Assuming that the viscous coefficient is proportional to

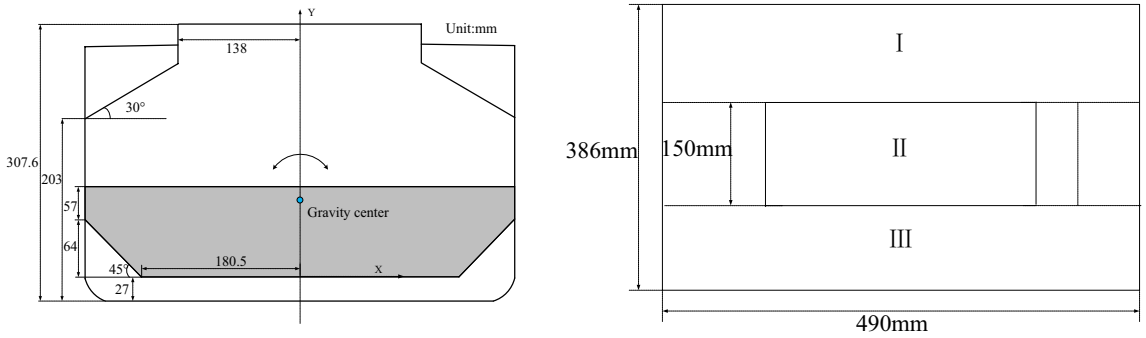

Fig. 17 Side view of tank II (left) and top view of the vessel (right)

Table 4 Loading conditions and mass settings for the calculations

Description	Parameters
Depth of loading d (mm)	121
Mass of cargo (kg)	14.0
Mass of the vessel excluding the cargo (kg)	18.2
Length of tank II (mm)	150
Length of the vessel (mm)	386
Width of the vessel (mm)	490
Draft of the vessel (mm)	171.2
Height of gravity center above the inner bottom	80
Rotational inertia of rolling (kg m^2)	0.884

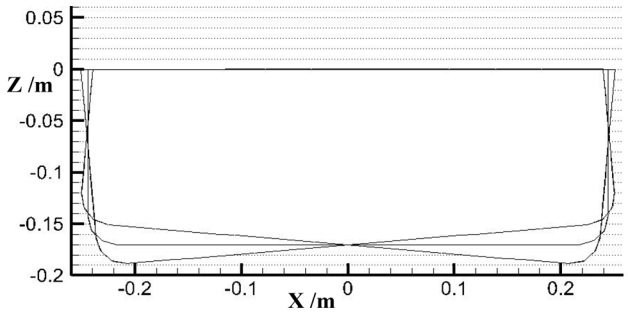

Fig. 18 The underwater parts of the vessel under different initial heeling angles

the angular velocity, the formula of the viscous coefficient can be presented as follows [12].

$$b_{44} = 2\varepsilon\sqrt{m_{44} + a_{44}(\infty)c_{44}}. \quad (10)$$

Here ε is a constant usually decided empirically. Its recommended value is in the range of 0.02–0.10 [12, 37]. In the present study, its value is set to 0.024. And $a_{44}(\infty)$ is the added mass of the roll motion at infinite frequency.

Based on the coupling strategy presented in Fig. 1, the hydrodynamic coefficients should be calculated first. The underwater parts of the vessel with different initial heeling angles are shown in Fig. 18. The mesh adopted in the BEM calculation when the vessel is at upright position is presented in Fig. 19. The hydrodynamic coefficients of the vessel with different initial heeling angles are shown in Fig. 20. Based on the above results, the computation of the coupled roll motion of the vessel loaded with liquefied cargo could be carried out.

4.2 Numerical tilting tests

To assess the weaken effect of liquefied cargo sloshing on a vessel's restoring ability quantitatively, a series of numerical tilting tests has been carried out. The tilting test is carried out based on the tank II loaded with liquefied cargo and it

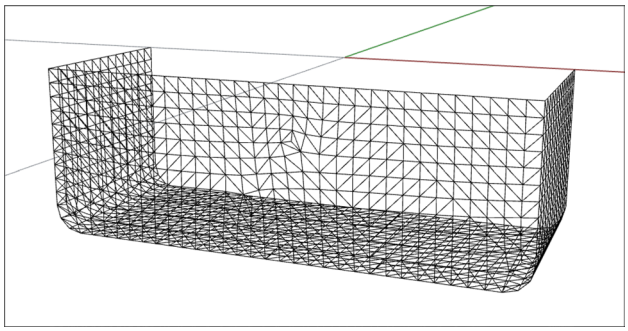

Fig. 19 The mesh adopted in the BEM calculation when the vessel is in upright position

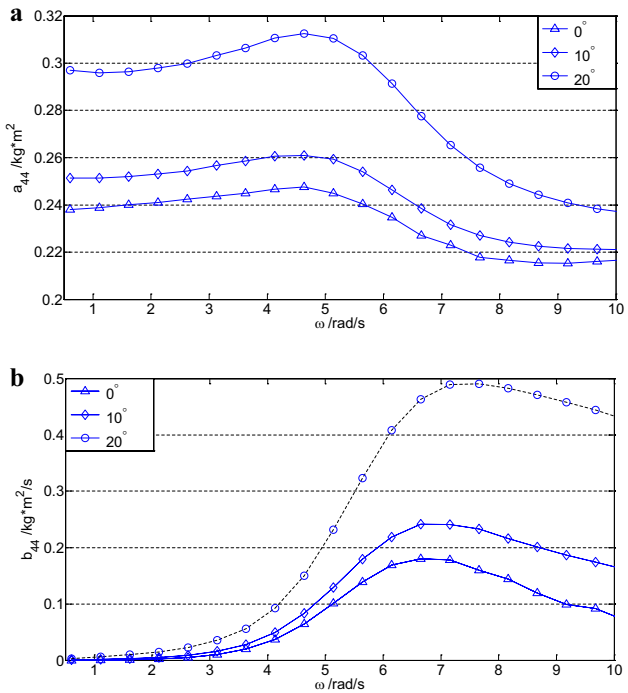

Fig. 20 The added mass (**a**) and damping coefficient (**b**) of the vessel under different initial heeling angles

tilts around the gravity center of the vessel. To account for the effect of different rolling speeds, three different tilting speeds are discussed, which are 1°/s, 10°/s and 15°/s, respectively. The maximum tilt angle is set to 50°. And the tilting starts from its equilibrium position.

The free surface deformation of liquefied nickel ore in the tank at different inclinations are shown in Figs. 21, 22, and 23. At a smaller tilting speed and as the tank tilts to the right, the liquefied cargo moves slowly to the right side of the tank. During the tilting, the interface does not change very much and it is almost parallel to the horizontal plane. When the tilting speed increases to 10°/s and 15°/s, the movement of the cargo gradually lags behind the

motion of the tank (see Figs. 21, 22). In general, the deformation of the interface is small, but its lag effect becomes apparent when the tilting speed increases.

The transverse offsets of the center of gravity of the liquefied cargo during the tilting tests are presented in Fig. 24. Based on the results, it can be seen that the transverse offset of the center of gravity increases gradually as the tank tilts to right. When the inclination is greater than 40°, the moving of the center of gravity becomes slowly for the constraint of the tank shape. Furthermore, when the tilting speed is bigger, the transverse offset becomes relatively smaller at the same inclinations because the lag effect becomes apparent. Considering the integrity, another tilting test of a full period is carried out with a speed of 10°/s. The snapshots of the test are shown in Fig. 25. Through the transverse offset of the center of gravity, the transverse offset of the vessel's center of gravity can be deduced. And the transverse offset of the center of gravity of the vessel corresponding to the reduction of its righting arm for it moves closer to its buoyancy line. Thus, the righting arm with or without considering the

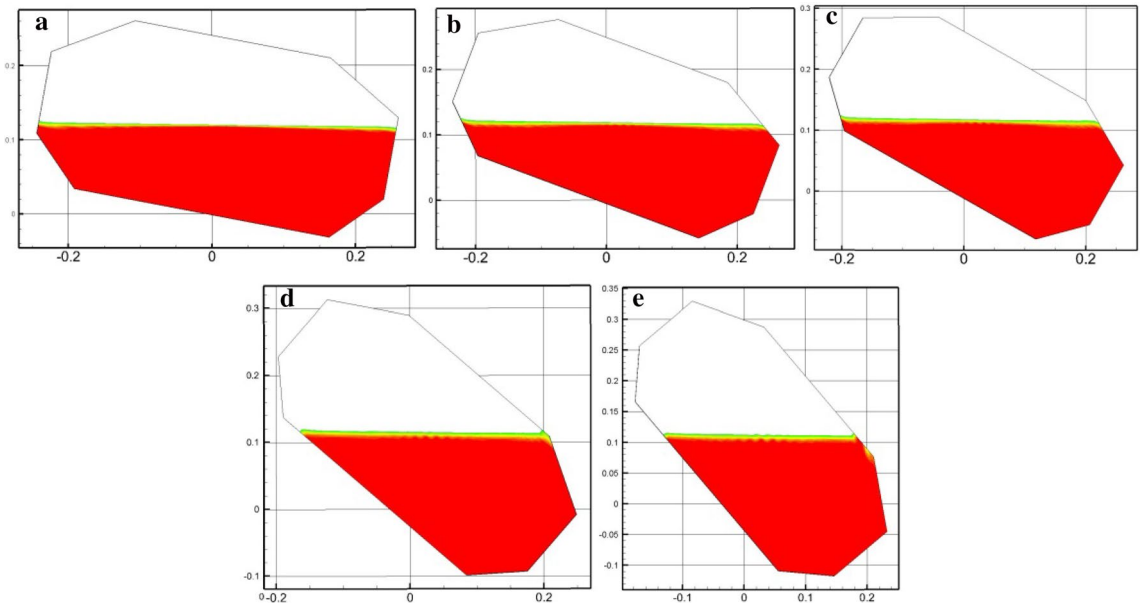

Fig. 21 Views of cargo in inclined tank at different inclinations, **a** 10°; **b** 20°; **c** 30°; **d** 40°; **e** 50° and the tilting rate is 1°/s

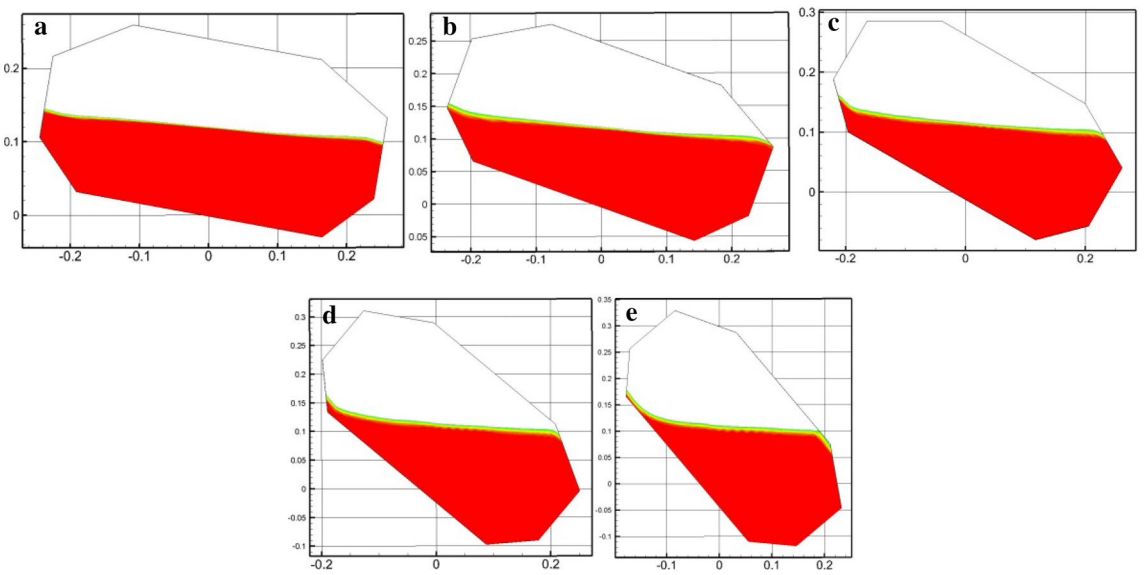

Fig. 22 Views of cargo in inclined tank at different inclinations, **a** 10°; **b** 20°; **c** 30°; **d** 40°; **e** 50° and the tilting rate is 10°/s

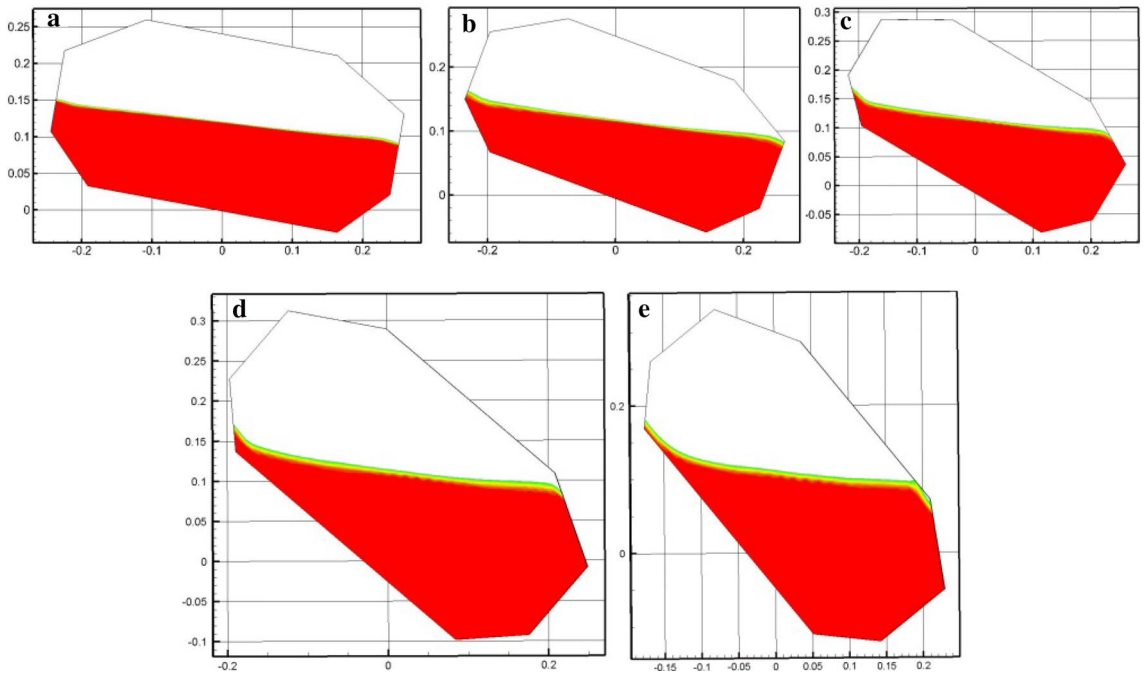

Fig. 23 Views of cargo in inclined tank at different inclinations, **a** 10°; **b** 20°; **c** 30°; **d** 40°; **e** 50° and the tilting rate is 15°/s

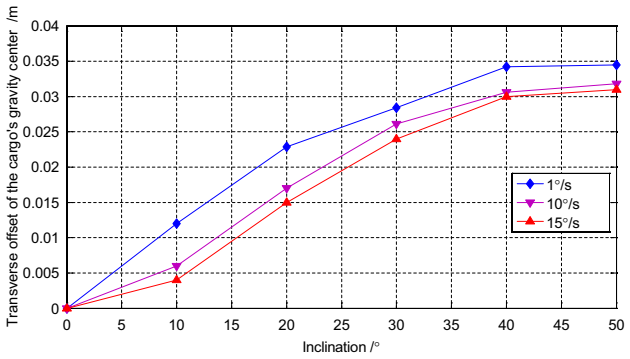

Fig. 24 Transverse offset of liquefied cargo gravity center as a function of model inclinations

sloshing of liquefied cargo can be estimated and presented in Fig. 26. It can be seen that the restoring ability is reduced once the movement of the cargo starts. When the inclination approaches 10°, the center of gravity of the cargo recoincides with its initial position and the weaken effect is reduced to zero. As the inclination becomes larger, the righting arm of the vessel is still reduced for the movement of the liquefied cargo. The area enclosed by the GZ curve and the horizontal axis is reduced to about 40% when considering the liquefied cargo. Therefore, the weaken effect of the liquefied cargo on the vessel is a key factor when carrying out the simulation of the coupled roll motion.

4.3 Coupled roll motion of the vessel in regular waves

It should be noted that the credibility of the present model relied on separate and coupled validations of the two solvers done in Sect. 3. Based on the coupled strategy and the database approach, the two effects the liquefied cargo sloshing are both included in the present simulation. Based on the wave theories described in Ref. [38] and considering the computation efficiency, the wave frequencies are set from 2.1162 to 7.1566 rad/s, and the wave amplitude is 0.05 m. At each wave frequency, the simulation lasts for ten periods. To facilitate understanding, the results only considering the sloshing-induced moment are also presented and compared. Taking four different wave frequencies, for example, time histories of the coupled roll motion of the vessel are shown in Figs. 27, 28, 29, and 30.

As shown in Fig. 27, when the wave frequency is 2.1162 rad/s, the left–right asymmetry occurs in the coupled roll motion considering both of the effects of the liquefied cargo. For the asymmetry of the roll response, the main reason lies in the asymmetry of the restoring ability. Due to the lag effect of the movement of the liquefied cargo, the righting arm is reduced at the same position compared to the case without considering cargo movement. Thus, the vessel rolls are smaller than the case without the cargo movement. When only the sloshing-induced moment is considered, the asymmetry does not happen and the amplitude of the roll motion is larger than the case considering both of the effects. The

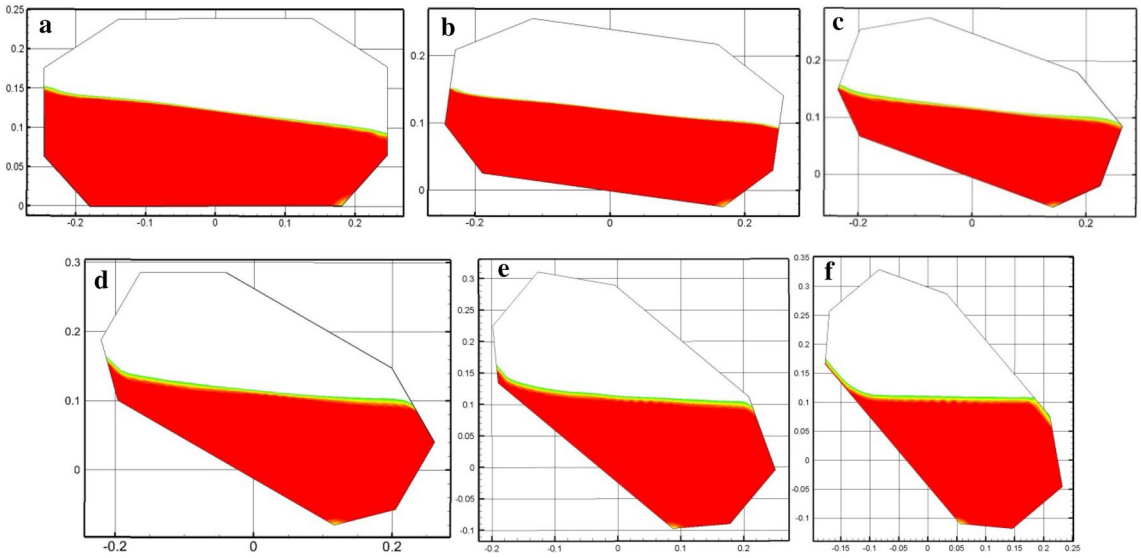

Fig. 25 Views of liquefied cargo returns from left to right at different inclinations, **a** 0°; **b** 10°; **c** 20°; **d** 30°; **e** 40°; **f** 50°. The tilting rate is 10°/s

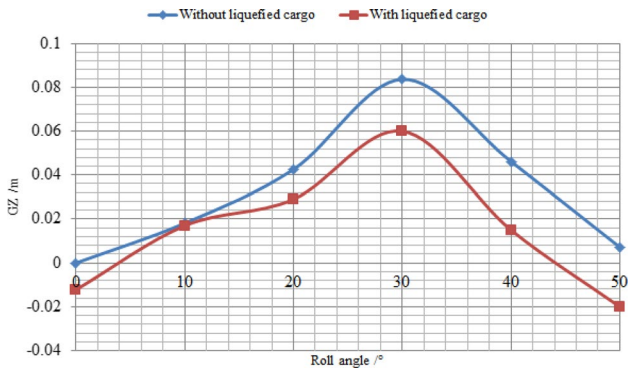

Fig. 26 The righting arm with or without considering the movement of liquefied cargo

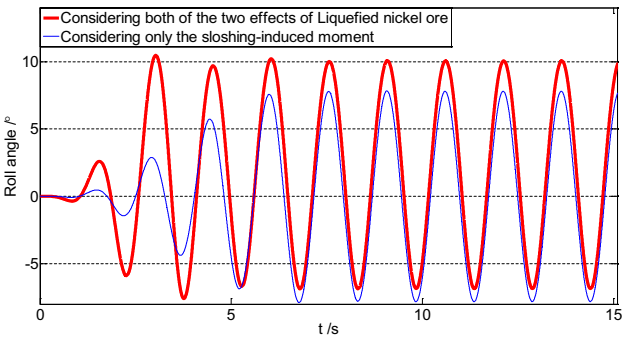

Fig. 28 Time history of the coupled roll motion when wave frequency is 4.1323 rad/s

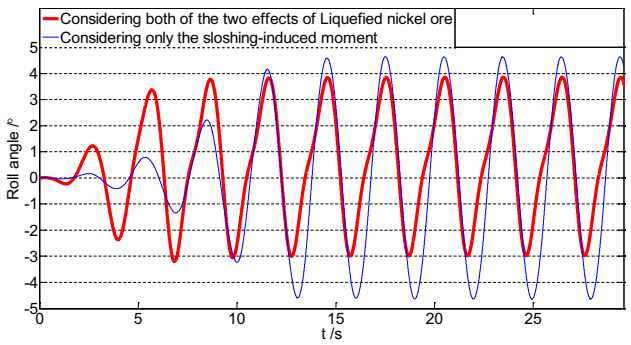

Fig. 27 Time history of the coupled roll motion when wave frequency is 2.1162 rad/s

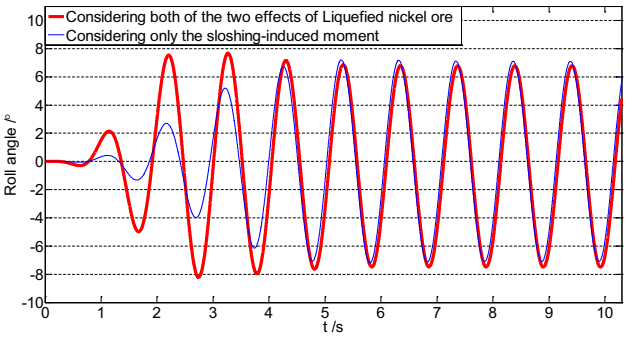

Fig. 29 Time history of the coupled roll motion when wave frequency is 6.1485 rad/s

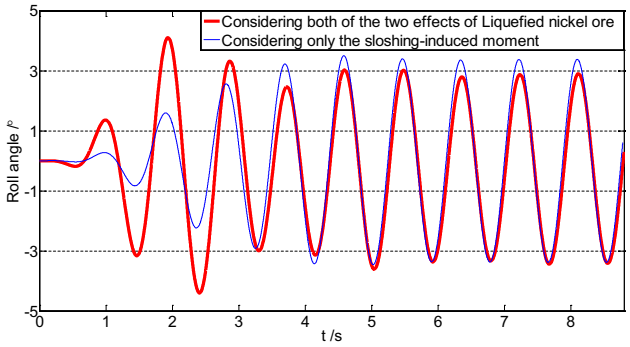

Fig. 30 Time history of the coupled roll motion when wave frequency is 7.1566 rad/s

reason is that the sloshing-induced moment plays a major role in the coupled case compared to the weaken effect of the liquefied cargo and the sloshing-induced moment plays a role in increasing the roll motion at the moment. As the wave frequency approaches the resonance frequency (see Fig. 28), the left–right asymmetry becomes apparent for the case considering both of the effects. As the wave frequency increases further (see Figs. 29, 30), the asymmetry still appears. The degree of the asymmetry of the coupled roll motion at different wave frequencies is shown in Fig. 31. From the results, it can be seen that the asymmetry always occurs and its value reaches maximum at the resonance region.

To further investigate the effect of the liquefied cargo, variations of the coupled roll motion at larger wave amplitude were simulated. Three different wave frequencies are chosen for the analysis, which are 2.1162 rad/s, 4.1323 rad/s and 5.1404 rad/s, respectively. Two of the wave frequencies are near and the other two are beyond the resonance region. The wave amplitude is set to 0.15 m. Time histories of the coupled roll motion under the four wave frequencies are shown in Figs. 32, 33, and 34.

From Figs. 32, 33, and 34, it can be seen that the asymmetry is intensified when the external wave amplitude becomes bigger. Especially, when the wave frequency is lower than or

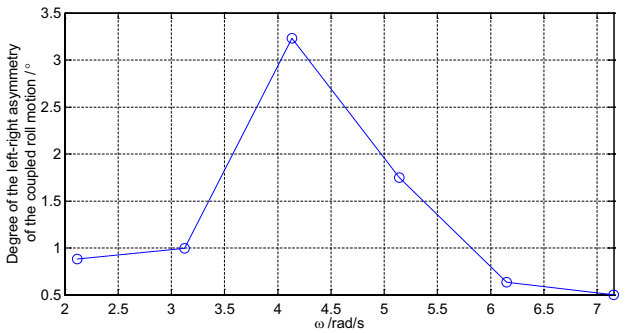

Fig. 31 The left–right asymmetry at different wave frequencies

in the resonance region, the asymmetry is most pronounced. When the wave frequency is 4.1323 rad/s (see Fig. 33), the simulation of the motion suspended at its seventh period. And the roll angle reaches a maximum of 44.2°. The restoring coefficient of the vessel decreases to zero at the same time (see Fig. 35). At that moment, the vessel rolls to the maximum angle and its restoring ability decreases to the minimum. Therefore, the vessel loses its ability to recover and the capsizing could happen when some other disturbances added.

Based on the above results, it can be seen that the vessel loaded with liquefied cargo experiences large amplitude roll motion under the conditions of larger wave amplitudes and the resonance wave frequency. Furthermore, the coupled roll motion becomes asymmetric for the weaken effect of the liquefied cargo on its restoring ability. Moreover, the asymmetric roll motion of the vessel is intensified because of the asymmetric movement of the liquefied cargo in the cargo hold. The capsizing of the vessel can happen directly in some severe seas. And it may happen in other cases owing to the complexity of the real navigational environment.

5 Conclusions

In the present study, the coupled effect of liquefied nickel ore sloshing on the rolling response of a vessel in waves is numerically investigated based on a prismatic cargo hold fixed on a box-type vessel. A numerical model based on a CFD solver and non-Newtonian constitutive equations was established to solve the sloshing problem of liquefied nickel ore. The simplified body surface nonlinear method is employed for the external ship response. The two problems are coupled through a coupling strategy. Two examples with and without considering the internal sloshing are carried out and compared with available experimental data. The comparisons show good agreement. To include the weaken effect

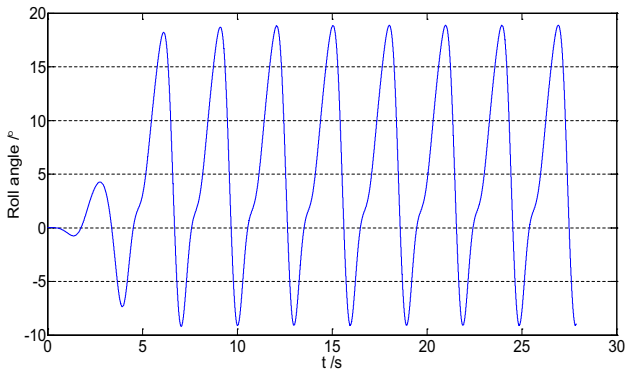

Fig. 32 Time history of the coupled roll motion when wave frequency is 2.1162 rad/s

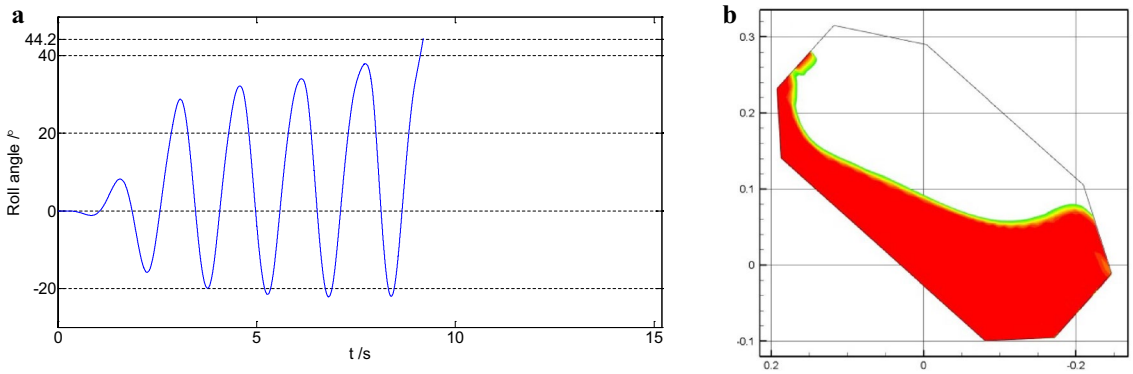

Fig. 33 Time history of the coupled roll motion when wave frequency is 4.1323 rad/s (**a**) and view of the situation corresponding to the roll angle of 44.2° (**b**)

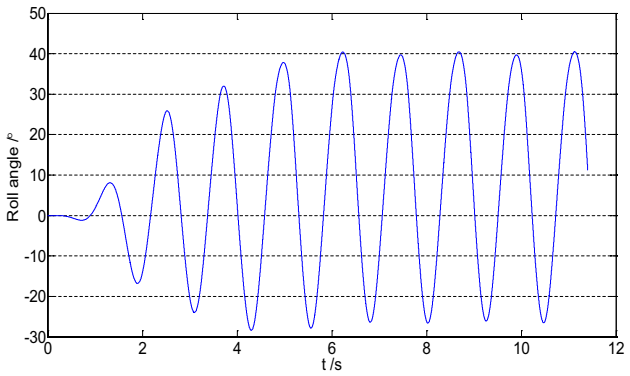

Fig. 34 Time history of the coupled roll motion when wave frequency is 5.1404 rad/s

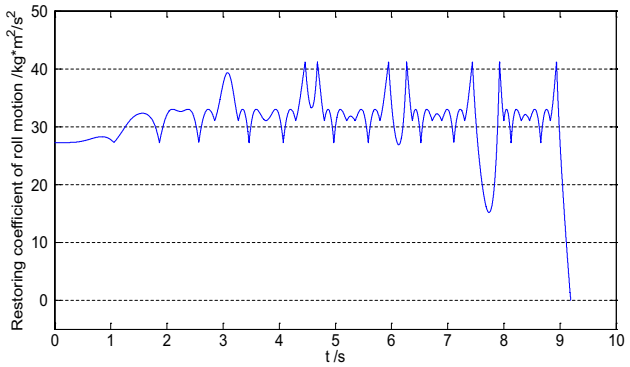

Fig. 35 Time history of the restoring coefficients when wave frequency is 4.1323 rad/s

of the liquefied nickel ore on the restoring ability of the vessel, the numerical tilting tests were carried out. Finally, simulation of the coupled roll motion of a vessel loaded with liquefied nickel ore is carried out and the following conclusions could be made.

1. Based on the numerical results, the model established in the present study is capable of dealing with the two effects of sloshing-induced moment and the weaken effect of the cargo on the restoring ability of a vessel.
2. According to the numerical tilting tests, the righting arm of the vessel is reduced once the movement of liquefied nickel ore begins and the area enclosed by GZ curve and the horizontal axis is reduced about 40% considering the movement of the liquefied cargo. Thus, the weaken effect of the liquefied nickel ore on the restoring ability is an important factor to be considered in the coupled analysis.
3. Though the wave amplitude is small, the left–right asymmetry appears in the coupled roll motion of the vessel. And the asymmetry becomes apparent when the wave frequency is in the resonance region. As the wave amplitude becomes larger, the asymmetry of the coupled roll motion intensifies. When the wave frequency is 4.1323 rad/s, the rolling response of the vessel continues to increase till the roll angle reaches the maximum, at which time its restoring ability decreases to zero and the restoring ability is lost. Thus, the larger wave amplitude and the resonance wave frequency combined with the weakened restoring ability of the liquefied cargo sloshing are the main reasons for the capsizing of a bulk carrier in real conditions.

In the present study, the liquefied cargo with 40% moisture content is assumed as a single-phase non-Newtonian fluid with the uniform rheology. In reality, layers with different characteristics would appear during the liquefaction process. Thus, more accurate constitutive equations are the focus of the future research to describe its stress–strain relationship. Furthermore, the characteristics of the actual liquefied cargo would be different in the model scale simulation. And when considering the scale effect of the cargo, perhaps its movement would intensify which should be studied

further to assess its coupled effect on vessel motions more accurately.

Acknowledgements Support for this research was provided by the National Natural Science Foundation of China under Award no. 51809237.

References

1. International Maritime Organisation (2013) International maritime solid bulk cargoes code (IMSBC Code) and supplement. 2013 Edn. ISBN 978-92-801-1587-1
2. Lee HL (2017) Nickel ore bulk liquefaction a handymax incident and response. Ocean Eng 139:65–73
3. INTERCARGO (2016) Bulk Carrier Casualty Report
4. Xiaonan C, Minyan L, Longjun H (2014) Shipwreck statistical analysis and suggestions for ships carrying liquefiable solid bulk cargoes in China. Proc Eng 84:188–194
5. Bačkalov I, Bulian G, Cichowicz J, Eliopoulou E, Konovessis D, Leguen J-F et al (2016) Ship stability, dynamics and safety: status and perspectives from a review of recent STAB conferences and ISSW events. Ocean Eng 116:312–349
6. Vassalos D, Francescutto A, Neves M (2016) Special issue on the stability of ships and ocean vehicles. Ocean Eng 125:349–351
7. Koromila IA, Spandonidis CC, Spyrou KJ (2013) Experimental investigation of cargo liquefaction and impact on the stability of a bulk—carrier. In: Proceedings of the 13th international ship stability workshop. Brest
8. Spandonidis CC, Spyrou KJ (2016) Coupled vessel-dry-granular-cargo roll dynamics in regular beam seas. Ocean Eng 120:238–245
9. Ju L, Xue Y, Vassalos D, Liu Y, Ni B (2017) Numerical investigation of rolling response of a 2D rectangular hold, partially filled with moist bulk cargo. Ocean Eng 142:348–362
10. Faltinsen OM, Timokha AN (2009) Sloshing. Cambridge University Press, New York
11. Kim Y (2002) A numerical study on sloshing flows coupled with ship motion—the anti-rolling tank problem. J Ship Res 46:52–62
12. Kim Y, Nam BW, Kim DW, Kim YS (2007) Study on coupling effects of ship motion and sloshing. Ocean Eng 34:2176–2187
13. Lee SJ, Kim MH, Lee DH, Kim JW, Kim YH (2007) The effects of LNG-tank sloshing on the global motions of LNG carriers. Ocean Eng 34:10–20
14. Li Y-L, Zhu R-C, Miao G-P, Fan J (2012) Simulation of tank sloshing based on OpenFOAM and coupling with ship motions in time domain. J Hydrodyn Ser B. 24:450–457
15. Jiang S-C, Teng B, Bai W, Gou Y (2015) Numerical simulation of coupling effect between ship motion and liquid sloshing under wave action. Ocean Eng 108:140–154
16. Rognebakke OF, Faltinsen OM (2003) Coupling of sloshing and ship motions. J Ship Res 47:208–221
17. Nasar T, Sannasiraj SA, Sundar V (2010) Motion responses of barge carrying liquid tank. Ocean Eng 37:935–946
18. Zhao W, Yang J, Hu Z (2012) Effects of sloshing on the global motion responses of FLNG. Ships Offshore Struct 8:111–122
19. Zhao W, Yang J, Hu Z, Xiao L, Tao L (2014) Hydrodynamics of a 2D vessel including internal sloshing flows. Ocean Eng 84:45–53
20. Ju L, Vassalos D, Boulougouris E (2016) Numerical assessment of cargo liquefaction potential. Ocean Eng 120:383–388
21. Zhang J, Wu W, Hu J (2016) A numerical study of the effects of the longitudinal baffle on nickel ore slurry sloshing in a prismatic cargo hold. Mar Struct 46:149–166
22. Bakker CW, Meyer CJ, Deglon DA (2009) Numerical modelling of non-Newtonian slurry in a mechanical flotation cell. Miner Eng 22:944–950
23. Bakker CW, Meyer CJ, Deglon DA (2010) The development of a cavern model for mechanical flotation cells. Miner Eng 23:968–972
24. Tseng WJ, Chen C-N (2003) Effect of polymeric dispersant on rheological behavior of nickel–terpineol suspensions. Mater Sci Eng A 347:145–153
25. Oliveira PJ, Pinho FT, Pinto GA (1998) Numerical simulation of non-linear elastic flows with a general collocated finite-volume method. J Nonnewton Fluid Mech 79:1–43
26. ANSYS/Fluent (2012) Fluent User's Guide: Ansys Inc
27. Gao Z, Gao Q, Vassalos D (2013) Numerical study of damaged ship flooding in beam seas. Ocean Eng 61:77–87
28. Fonseca N (1998) Time-domain analysis of large amplitude vertical ship motions and wave loads. J Ship Res 42:139–153
29. Fonseca N, Soares CG (2005) Validation of a time-domain strip method to calculate the motions and loads on a fast monohull. Appl Ocean Res 26:256–273
30. ECN (2014) LHEEA—Nemoh
31. Sheng W, Alcorn R, Lewis A (2015) A new method for radiation forces for floating platforms in waves. Ocean Eng 105:43–53
32. Schmitt P, Windt C, Nicholson J, Elsässer B (2016) Development and validation of a procedure for numerical vibration analysis of an oscillating wave surge converter. Eur J Mech B Fluids 58:9–19
33. Hashimoto H, Ito Y (2012) Numerical Simulation Method for Coupling of Tank Fluid and Ship Roll Motions. In: Proceedings of the 11th international conference on the stability of ships and ocean vehicles (STAB 2012). Athens. pp 477–485
34. Chen Y (2013) Experimental study on capsizing mechanism of nickel ore carrier [Master]. Harbin Engineering University, Harbin
35. Guan C, Dong G, Gao J, Jin Y (2014) Platform experiment and research of nickel ore liquefaction process. Chin J Hydrodyn 29:700–705
36. Zhou J, Zhu Y, Jian Q, Jia M, Jin Y (2014) Modeling Experiments on the Fluidization of Laterite nickel Ore in Bulk. Chin J Geotech Eng 36:1515–1520
37. Gou Y, Kim Y, Kim T-Y (2011) A numerical study on coupling between ship motions and sloshing in frequency and time domains. In: Proceedings of the twenty-first (2011) international offshore and polar engineering conference
38. Mehaute BL (1976) An introduction to hydrodynamics and water waves. Springer, Singapore